SCIENTIFIC REPORTS

OPEN

Manganese Phosphate Self-assembled Nanoparticle Surface and Its application for Superoxide Anion Detection

Received: 02 February 2016
Accepted: 08 June 2016
Published: 30 June 2016

Xiaohui Shen, Qi Wang, Yuhong Liu, Wenxiao Xue, Lie Ma, Shuaihui Feng, Mimi Wan, Fenghe Wang & Chun Mao

Quantitative analysis of superoxide anion ($O_2^{\cdot-}$) has increasing importance considering its potential damages to organism. Herein, a novel Mn-superoxide dismutase (MnSOD) mimics, silica-manganous phosphate (SiO_2-$Mn_3(PO_4)_2$) nanoparticles, were designed and synthesized by surface self-assembly processes that occur on the surface of silica-phytic acid (SiO_2-PA) nanoparticles. The composite nanoparticles were characterized by fourier transform infrared spectroscopy (FTIR), transmission electron microscopy (TEM), scanning electronic microscopy (SEM), electron diffraction pattern, energy dispersive spectroscopy (EDS) and elemental mapping. Then the electrochemical measurements of $O_2^{\cdot-}$ based on the incorporation of SiO_2-$Mn_3(PO_4)_2$ onto the surface of electrodes were performed, and some satisfactory results were obtained. This is the first report that manganous phosphate ($Mn_3(PO_4)_2$) nanoparticles with shape-controlled, but not multilayer sheets, were utilized for $O_2^{\cdot-}$ detection. The surface self-assembly technology we proposed will offer the ideal material to construct more types biosensor and catalytic system for its nanosized effect.

Active reactive oxygen species (ROS) containing oxygen atoms are the substances with strong oxidizing ability, which can cause or aggravate cancer, cardiovascular diseases, asthma, cataract, ulcer disease, Alzheimer's disease, Parkinson's disease and other diseases. $O_2^{\cdot-}$, the critical important part of the so-called ROS, is implicated in many physiological and pathological processes[1–3]. Under normal physiological conditions, $O_2^{\cdot-}$ maintains the relatively balanced level *in vivo*. Once the cell produces excessive $O_2^{\cdot-}$ in response to external stimulus or pathological changes, it will lead to etiology of aging, cancer, and progressive neurodegenerative diseases such as Parkinson's disease. Thus, real-time analysis and detection of $O_2^{\cdot-}$ have great significance. A variety of approaches have been tried to measure $O_2^{\cdot-}$ concentration, such as electron spin resonance[4–6], spectrophotometry[7], chemiluminescence[8], colorimetry[9,10], chromatograph[11,12] and fluorescence[13–15]. However, these methods cost much and usually occupy too much space. In comparison with other methods, the electrochemical method has recently attracted a great deal of attention owing to its advantages including high sensitivity, low detection limit, simplicity, direct, real-time detection and so on.

Up to date, the commonly used electrochemical enzyme sensors are fabricated by immobilizing superoxide dismutase (SOD) and cytochrome (cyt c) onto the electrode surface. However, the enzymatic $O_2^{\cdot-}$ sensors are easily affected by pH and temperature changes, which limit their practical applications due to the poor stability of nature enzyme. Nanozymes, possessing enzymatic activities with nanostructure, have attracted particular attention as emerging natural enzyme mimics, they offer the possibility of lowered cost, improved stability, and excellent recyclability[16–18]. Meanwhile, bionic concept has gained more and more attention[19–21]. Mn-superoxide dismutase (MnSOD) mimics, manganous phosphate ($Mn_3(PO_4)_2$), manganous pyrophosphate ($Mn_2P_2O_7$) and manganese (II) complexes are usually used to fabricate biosensors for $O_2^{\cdot-}$ detection[22,23]. Cabelli have studied the antioxidant mechanism of aggregated $Mn_3(PO_4)_2$ particles in organic vivo[24]. Li used DNA as a template to

National and Local Joint Engineering Research Center of Biomedical Functional Materials, Jiangsu Key Laboratory of Biofunctional Materials, School of Chemistry and Materials Science, Nanjing Normal University, Nanjing, 210023, China. Correspondence and requests for materials should be addressed to M.W. (email: wanmimi@njnu.edu.cn) or C.M. (email: maochun@njnu.edu.cn)

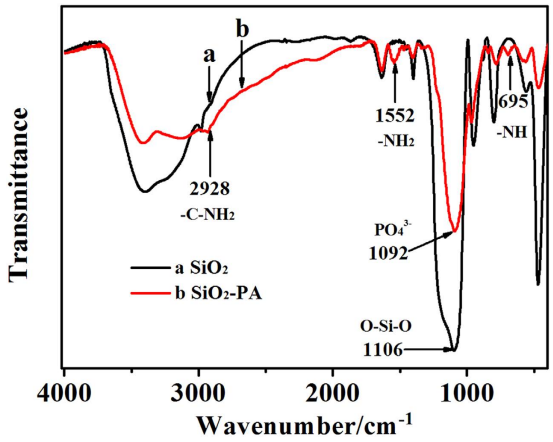

Figure 1. FTIR spectra of (**a**) SiO_2 NPs, and (**b**) SiO_2-PA NPs.

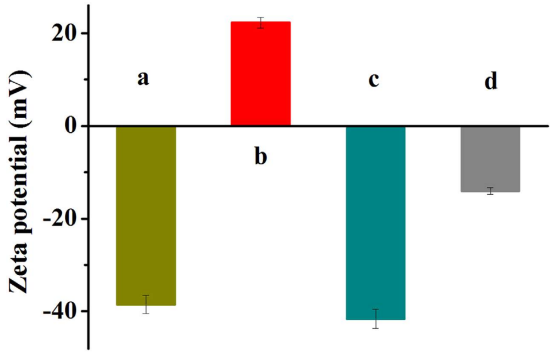

Figure 2. (**a**) SiO_2 NPs, (**b**) SiO_2-NH_2 NPs, (**c**) SiO_2-PA NPs, and (**d**) SiO_2-$Mn_3(PO_4)_2$ NPs of Zeta potential analysis.

produce $Mn_3(PO_4)_2$ nanosheets and decorated this biomimetic enzyme onto the electrode surface for sensitive *in-situ* detection of $O_2^{\cdot -}$[25]. However, the intrinsic drawbacks of DNA, including high cost, instability, and storage difficulty, may limit their widely applications of electrochemical sensors. Dai also reported the high efficient catalysis of $Mn_2P_2O_7$, which was used as a SOD mimic for $O_2^{\cdot -}$ detection[26]. There is a serious problem in dealing with the preparation of these reported MnSOD mimics. It is that the conventional synthesized MnSOD mimics that reported in the previous literatures have multilayer sheet structure with uncontrolled shape, thickness and size. This approach will bring resources waste and low catalytic efficiency. We wonder how it is possible to utilize surface self-assembly technology and nanotechnology to construct a more efficient MnSOD mimic for promoting analytical properties.

In this paper, SiO_2-$Mn_3(PO_4)_2$ NPs were synthesized by surface self-assembly processes that occur on the surface of SiO_2-phytic acid (SiO_2-PA). To the best of our knowledge, there are no reports employing surface coating technique to immobilize $Mn_3(PO_4)_2$ onto the surface of NPs for $O_2^{\cdot -}$ detection. The SiO_2-$Mn_3(PO_4)_2$ NPs have many advantages, like controllable shape with nanoscale, high specificsurface area than that of nano-sheet structure, low cost, simple preparation process, non-toxic, and so on. This novel MnSOD mimic we prepared is utilized to fabricate biosensors, and the electrochemical measurements of $O_2^{\cdot -}$ based on the incorporation of SiO_2-$Mn_3(PO_4)_2$ onto the electrodes surface are performed.

Results and Discussion

Figure 1 showed the fourier transform infrared (FTIR) spectroscopy of SiO_2 NPs (a) and SiO_2-PA NPs (b). For curve (a), the appearance of characteristic peak at 1106 cm^{-1} and 957 cm^{-1} were attributed to the O-Si-O bonds stretching vibration, indicating that SiO_2 NPs were successfully synthesized[27]. Compared with unmodified SiO_2 NPs, the SiO_2-PA NPs illustrated three extra peaks at 2928, 1552 and 695 cm^{-1}, which should be attributed to -C-NH_2 stretching, symmetric -NH_2 stretching, and the bending vibrations of -NH in APTES, respectively[28]. The results indicated that APTES was successfully modified onto the surface of SiO_2 NPs[29]. More importantly, an adsorption peak at 1092 cm^{-1} was observed due to the overlap of the characteristic peak of phosphate group (PO_4^{3-}) and the peak of asymmetric O-Si-O stretching[30]. The results confirmed that the SiO_2 NPs were successfully modified by APTES and PA.

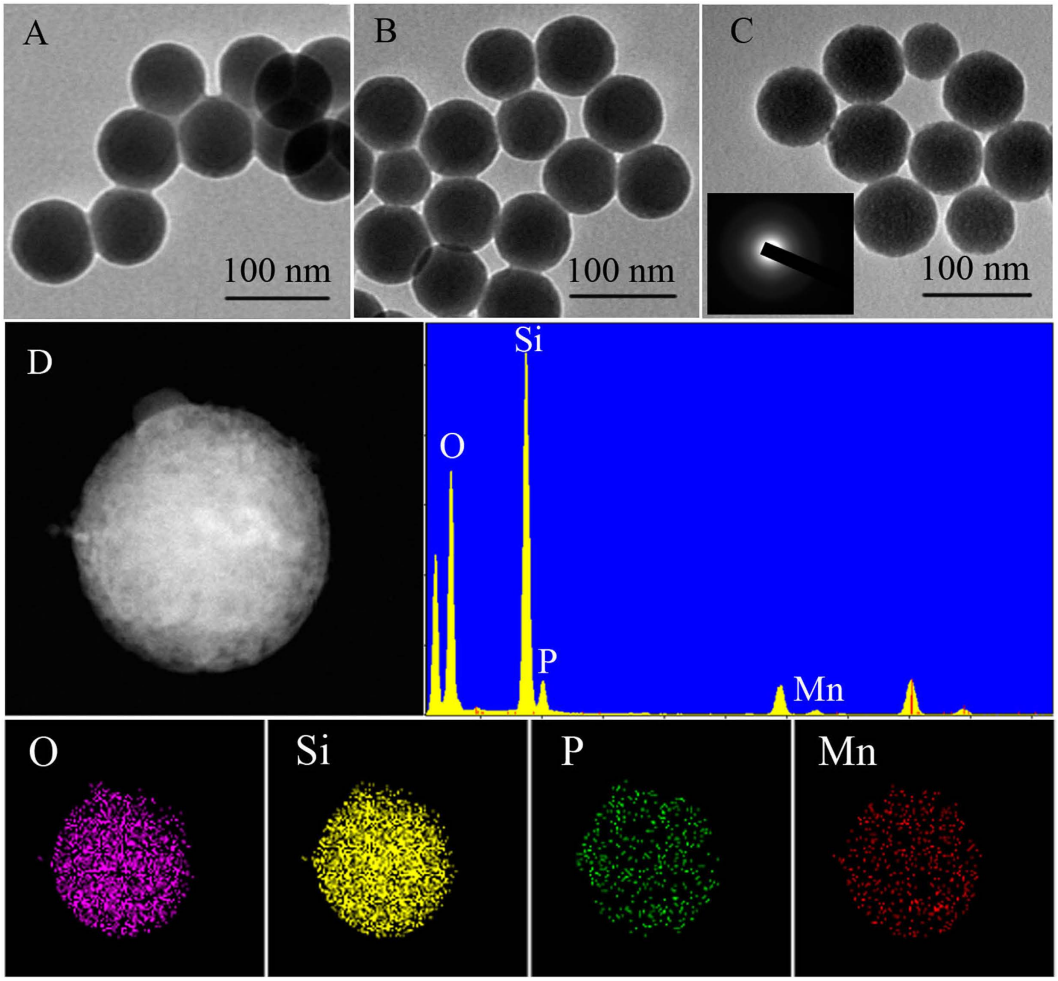

Figure 3. TEM images of (**A**) SiO_2 NPs, (**B**) SiO_2-PA NPs, (**C**) SiO_2-$Mn_3(PO_4)_2$ NPs, and (**D**) EDS spectrum and elemental mapping of SiO_2-$Mn_3(PO_4)_2$ NPs.

As shown in Fig. 2a, the Zeta potential of SiO_2 surface was −38.5 mV, which was attributed to many -OH and other oxygen-containing groups that present in the SiO_2 NPs surface. When modified with APTES, the Zeta potential of APTES-SiO_2 NPs increased to +22.3 mV that due to the amine groups on the surface of the particles (Fig. 2b). However, the Zeta potential measurements for SiO_2-PA NPs (Fig. 2c) showed a negative surface charge that owing to the six phosphate groups of PA. When Mn^{2+} ions in solution were self-assembled onto the surface of SiO_2-PA NPs, the zeta potential increased to −14.1 mV. The change of Zeta potential indicated that SiO_2-$Mn_3(PO_4)_2$ NPs were successfully synthesized by self-assembly technology based on the electrostatic interaction that between Mn^{2+} ions and the phosphate groups[31].

The TEM and SEM images were also employed to further confirm the formation of SiO_2-$Mn_3(PO_4)_2$ NPs. Figure 3A revealed that the spherical SiO_2 NPs were obtained with the average particle size of 75 nm. After surface self-assembly of PA and Mn^{2+} sequentially, the two sizes of SiO_2-PA NPs and SiO_2-$Mn_3(PO_4)_2$ NPs showed a slight increase (Fig. 3B,C), respectively. Furthermore, the electron diffraction pattern displayed an amorphous diffraction pattern of $Mn_3(PO_4)_2$ that deposited on the surface of silica (see the inset from Fig. 3C). And the corresponding elemental mapping of oxygen (O), silicon (Si), phosphorus (P), and manganese (Mn) from the SiO_2-$Mn_3(PO_4)_2$ NPs were indicated in Fig. 3D. The energy dispersive spectroscopy (EDS) of SiO_2-$Mn_3(PO_4)_2$ NPs showed that the different atomic percentages were 85.32% (O), 13.10% (Si), 1.47% (P), and 0.11% (Mn), respectively. It can be concluded that $Mn_3(PO_4)_2$ was firmly coated onto the outer surface of the SiO_2-PA NPs. $Mn_3(PO_4)_2$ layer has little effect on the size growth of SiO_2 NPs because it was only monolayer of $Mn_3(PO_4)_2$ molecular that self-assembled onto the outer surface of SiO_2 NPs based on the electrostatic interaction. Here, the stability of $Mn_3(PO_4)_2$ supported on SiO_2 NPs was evaluated by Zeta potential measurement after three weeks of storage. As was shown in Figure S1, the Zeta potential of the SiO_2-$Mn_3(PO_4)_2$ NPs had almost no change after three weeks of storage, indicating the $Mn_3(PO_4)_2$ NPs have long-term stability. SEM images were also used to investigate the surface texture change after $Mn_3(PO_4)_2$ coating on SiO_2 NPs, and the particle size of $Mn_3(PO_4)_2$. Figure S2 showed the SEM images of the SiO_2 NPs, SiO_2-PA NPs and SiO_2-$Mn_3(PO_4)_2$ NPs, respectively. It can be observed from the SEM results that the samples with $Mn_3(PO_4)_2$ coating can remain its original spherical morphology. Meantime, it can also be seen in this figure that particle size of the samples showed a slight increase after $Mn_3(PO_4)_2$ coating on SiO_2 NPs, which was in consistence with the results obtained by TEM images as showed

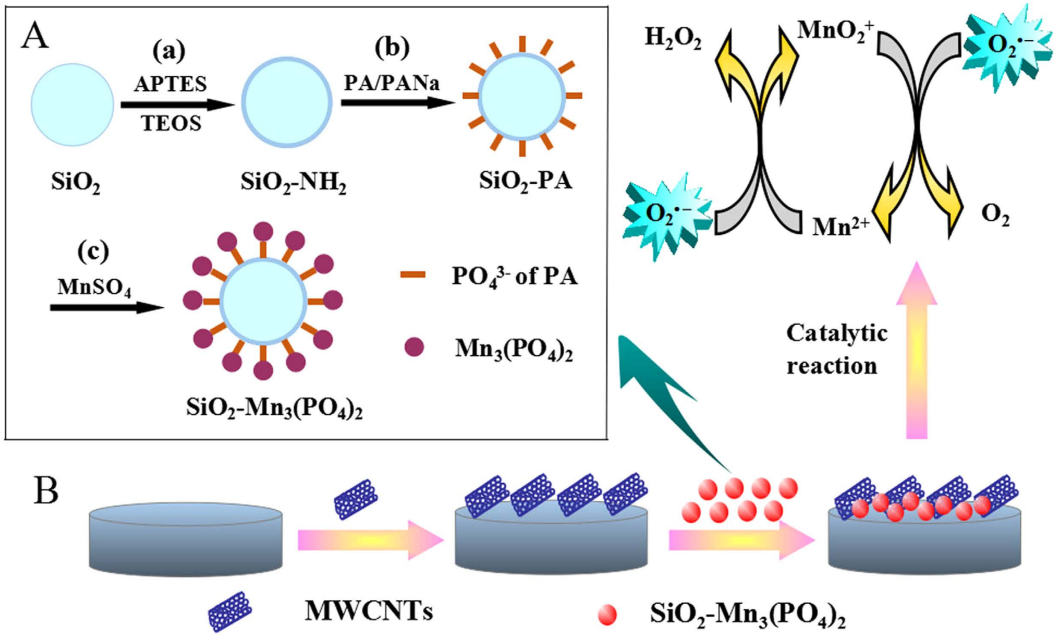

Figure 4. (**A**) Schematic illustration of the formation of SiO_2-$Mn_3(PO_4)_2$ NPs: (a) Amino-modified process of SiO_2 NPs, (b) Phytic acid modified process of SiO_2-NH_2 NPs, and (c) Self-assembled of $Mn_3(PO_4)_2$ on the outer surface of SiO_2-PA NPs, (**B**) Schematic diagram for the construction of the biosensor.

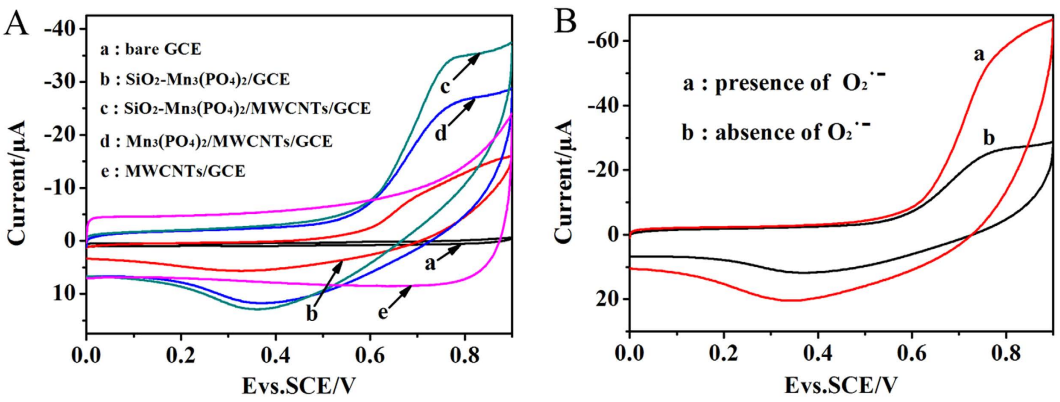

Figure 5. (**A**) Cyclic voltammograms (CVs) of (a) bare GCE, (b) SiO_2-$Mn_3(PO_4)_2$/GCE, (**c**) SiO_2-$Mn_3(PO_4)_2$/MWCNTs/GCE, (d) $Mn_3(PO_4)_2$/MWCNTs/GCE, and (e) MWCNTs/GCE, (**B**) CVs of SiO_2-$Mn_3(PO_4)_2$/MWCNTs/GCE in the presence (a) and absence (b) of 1.0 μmol L^{-1} $O_2^{\cdot-}$ in PBS (pH 7.4), scan rate: 100 mV·s^{-1}.

in Fig. 3. Figure 4A illustrated the synthesis process of SiO_2-$Mn_3(PO_4)_2$ NPs. The formational mechanism of this biomimetic enzyme could be explained as follows: After dropping into $MnSO_4$ solution, PO_4^{3-} ions, derived from the surface of SiO_2-PA NPs, were in combination with Mn^{2+}ions by electrostatic interaction to form $Mn_3(PO_4)_2$. When the PO_4^{3-} ions were consumed, the monolayer of $Mn_3(PO_4)_2$ molecular was self-assembly on the outer surface of SiO_2-PA NPs with controllable morphology. In addition, only aggregated $Mn_3(PO_4)_2$ particles were observed in the absence of SiO_2 NPs with the same reaction conditions (Supplementary Figure S3).

A schematic drawing of the stepwise construction process of modified glassy carbon electrode (GCE) was described in Fig. 4B. The electrochemical properties of the SiO_2-$Mn_3(PO_4)_2$/Multi-walled carbon nanotubes (MWCNTs)/GCE were investigated by cyclic voltammetry (CV) and Electrochemical Impedance Spectroscopy (EIS)[32–35] (Supplementary Figure S4). Figure 5A displayed that all fabrication process of SiO_2-$Mn_3(PO_4)_2$/MWCNTs/GCE were carried out by CV in nitrogen saturated phosphate buffered solution (PBS) at a scan rate of 100 mV·s^{-1}. In the working potential range of 0–0.9 V, there was no electrochemical signal can be observed at the bare GCE (curve a). In contrast, the SiO_2-$Mn_3(PO_4)_2$/GCE exhibited a pair of weakly redox peaks (curve b). When the MWCNTs/GCE was modified with SiO_2-$Mn_3(PO_4)_2$ NPs, the oxidation-reduction peaks were more obviously observed (curve c) that due to the excellent electronic conductivity of MWCNTs (Supplementary Figure S5), and the sensitivity of this biosensor was largely improved[36]. Moreover, the peak currents of SiO_2-$Mn_3(PO_4)_2$/MWCNTs/GCE (curve c) were much larger than that of $Mn_3(PO_4)_2$/MWCNTs/GCE (curve d).

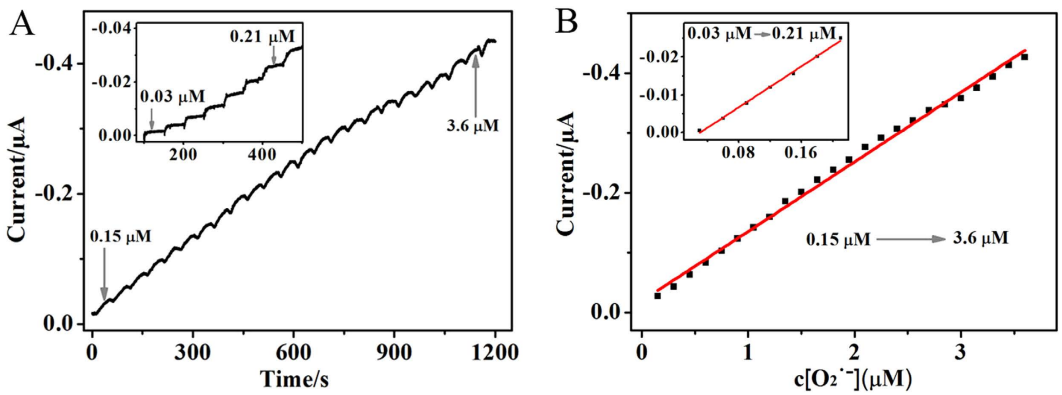

Figure 6. (**A**) Typical amperometric curve recorded at 0.484 V in PBS (pH 7.4) for SiO_2-$Mn_3(PO_4)_2$/MWCNTs/GCE, From 0.03 to 0.21 μM, the $O_2^{\cdot-}$ concentration of each adding step was 0.03 μM, from 0.15 to 3.6 μM, each adding step was 0.15 μM, (**B**) Linear calibration plot of the response current vs the $O_2^{\cdot-}$ concentration.

Results demonstrated that the electro-catalytic effect of SiO_2-$Mn_3(PO_4)_2$ was much higher than that of $Mn_3(PO_4)_2$ aggregated particles. It can be attributed to that the nanosized SiO_2-$Mn_3(PO_4)_2$ possessed high specific surface area. As a result, it will help improve the catalytic efficiency of $O_2^{\cdot-}$ in the electrolyte. When the bare GCE was only modified with MWCNTs, the background current was more clearly observed (curve e).

To study the catalysis effect of the SiO_2-$Mn_3(PO_4)_2$ NPs, the biosensor in PBS and PBS of containing 1.0 μmol L^{-1} $O_2^{\cdot-}$ were measured by CV, respectively. As shown in Fig. 5B, in the PBS containing of 1.0 μmol L^{-1} $O_2^{\cdot-}$ (curve a), both anodic and cathodic peak currents that corresponding to the redox reaction of in PBS (curve b) clearly increased that can be attributed to the oxidation and reduction of $O_2^{\cdot-}$, respectively[37]. According to the previous reports[38,39], $O_2^{\cdot-}$ was converted into O_2 and H_2O_2 during the disproportionation reaction that $O_2^{\cdot-}$ was catalyzed by Mn^{2+} in PBS. In the anodic process, $O_2^{\cdot-}$ was oxidized to O_2 by the oxidation effect of MnO_2^+, while MnO_2^+ was reduced to Mn^{2+}. On the contrary, Mn^{2+} was oxidized to MnO_2^+ in the cathodic process. As demonstrated above, the SiO_2-$Mn_3(PO_4)_2$/MWCNTs/GCE can be applied to detect $O_2^{\cdot-}$ by measuring the oxidation or reduction currents because of the high efficient catalysis of SiO_2-$Mn_3(PO_4)_2$. To further prove this proposed mechanism/reaction, X-ray photoelectron spectroscopy (XPS) analysis was carried out to analyze the composition and chemical configuration of the SiO_2-$Mn_3(PO_4)_2$ NPs before and after electrocatalysis process. More details about the XPS spectra of Mn 2p were presented in Figure S6.

The typical current-time plot of SiO_2-$Mn_3(PO_4)_2$/MWCNTs/GCE at the applied potential of 0.484 V upon successive additions of $O_2^{\cdot-}$ was provided in Fig. 6A. In this experiment, while being stirred, $O_2^{\cdot-}$ solution was added once per 50 seconds. With the injection of $O_2^{\cdot-}$, the response of this biosensor rapidly achieved 95% of the steady-state current within 2.9 s (Supplementary Figure S7). The SiO_2-$Mn_3(PO_4)_2$/MWCNTs/GCE showed a wide linear range from 0.03 to 0.21 μM and 0.15 to 3.6 μM with the correlation coefficient of 0.9966 and 0.9959, respectively. The relation of the oxidation peak current *vs* the concentration of $O_2^{\cdot-}$ was linear with a detection limit of 0.0175 μM (S/N = 3). The biosensor exhibited more excellent performance than some $O_2^{\cdot-}$ biosensors that reported by the previous papers using different electrode materials, such as SOD, $Mn_3(PO_4)_2$, and $Mn_2P_2O_7$ (Supplementary Table 1). The corresponding calibration curves for $O_2^{\cdot-}$ were depicted in Fig. 6B. The linear equations were i (μA) = 0.00418 − 0.1358c (μM) and i (μA) = −0.01932 − 0.1263c (μM), respectively. The biosensor was applied to the detection of $O_2^{\cdot-}$ and displayed excellent electrochemical behavior.

To verify the applicability of SiO_2-$Mn_3(PO_4)_2$ NPs in detection of $O_2^{\cdot-}$, Xanthine/Xanthine Oxidase (XAN/XOD) was selected to generate $O_2^{\cdot-}$ (Supplementary Figure S8). In addition, the response of SiO_2-$Mn_3(PO_4)_2$/MWCNTs/GCE toward $O_2^{\cdot-}$ generated by XAN/XOD was investigated by amperometric measurements[40]. As shown in Figure S9, with successive additions of XAN to the solution, a stepwise increase of the current response was observed.

To evaluate the anti-interference performance of detecting $O_2^{\cdot-}$, the biosensor was examined by successive additions of $O_2^{\cdot-}$ and interfering substances into a 0.1 M PBS at 0.484 V. Figure 7A indicated that there were obviously current responses of the biosensor during the addition of 1.0 μM $O_2^{\cdot-}$, while no obviously current response could be observed with the addition of the interferences. With the sequential addition of 5.0 μM Cys, 5.0 μM DA, 10 μM H_2O_2, 10 μM UA and 10 μM AA, the detection current showed changes of 14%, 2.7%, 8.2%, 5.4% and 4.1% with comparison of 1.0 μM $O_2^{\cdot-}$, respectively (Fig. 7B). Figure S10 displayed the amperometric response of the SiO_2-$Mn_3(PO_4)_2$/MWCNTs/GCE by successive additions of 2.0 μM 18-crown-6 once per 50 seconds. Results demonstrated that this biosensor can eliminate the interference and show an excellent selectivity for detection of $O_2^{\cdot-}$. To verify the stability, the biosensor was monitored after being stored for three weeks in a refrigerator. Figure 7C indicated that the current response was no apparent decrease, which was much longer than those obtained for enzyme-based $O_2^{\cdot-}$ biosensors[41–44]. In order to investigate the binding firmness of SiO_2-$Mn_3(PO_4)_2$ NPs decorated onto the MWCNTs/GCE electrode, the reuse ability of the SiO_2-$Mn_3(PO_4)_2$/MWCNTs/GCE electrode was tested. Figure S11 displayed the CV curves of the biosensor for 20 cycles, which showed almost overlap curves, indicating the biosensor we prepared had a good cycle stability that can attributed to the good binding state of the SiO_2-$Mn_3(PO_4)_2$ NPs and the MWCNTs/GCE electrode.

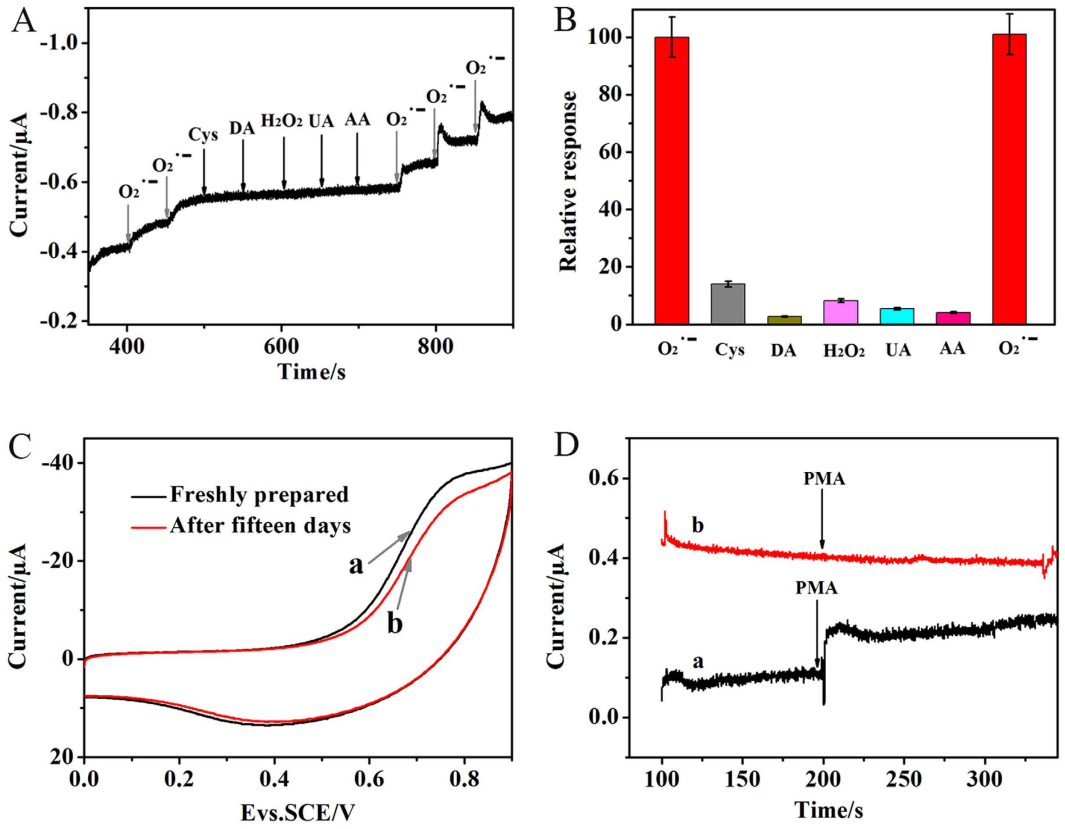

Figure 7. (**A**) Interference test of SiO_2-$Mn_3(PO_4)_2$/MWCNTs/GCE, (**B**) The relative response in PBS (pH = 7.4) at 1.0 μM $O_2^{\cdot-}$, 5.0 μM Cys, 5.0 μM DA, 10 μM H_2O_2, 10 μM UA and 10 μM AA, (**C**) CVs of SiO_2-$Mn_3(PO_4)_2$/MWCNTs/GCE, (a) Freshly prepared, and (b) after fifteen days in 0.1 M PBS, Scan rate was 100 mV·s^{-1}, and (**D**) Amperometric response of the SiO_2-$Mn_3(PO_4)_2$/MWCNTs/GCE in the (a) presence, and (b) absence of HeLa cells upon sequential additions of PMA to 0.1 M PBS at 0.484 V.

Real-time detection performance of the biomimetic enzyme sensor has also been monitored by detecting $O_2^{\cdot-}$ released from the HeLa cells. The amperometric responses of the biosensor were obtained at applied potentials of 0.484 V versus Ag/AgCl in 2 mL 0.1 M PBS (pH 7.4) containing 0.5×10^5 cells·mL^{-1}. After the injection of 4 μg mL^{-1} phorbol 12-myristate 13-acetate (PMA), which was reported to generate $O_2^{\cdot-}$ from live cells[45], the current gradually increased at SiO_2-$Mn_3(PO_4)_2$/MWCNTs modified electrode. In this work, PMA was used as a stimulant for the cell to exude $O_2^{\cdot-}$[46,47]. Figure 7D indicated that the strong current signal (0.01457 μA, curve a) was caused by $O_2^{\cdot-}$ released from the HeLa cells, considering that SiO_2-$Mn_3(PO_4)_2$ could selectively decomposes $O_2^{\cdot-}$. According to the above linear relationship, the $O_2^{\cdot-}$ concentration of 0.0765 μM was calculated. Thence, the amount of $O_2^{\cdot-}$ releasing from per 10^5 cells was calculated to be 0.153 nmol. Meanwhile, in the absence of the HeLa cells and the presence of the treatment of PMA, no obvious current response can be seen on the screen (curve b). To test the effectiveness of this technology, the biomimetic enzyme sensor has also been used to detect the concentration of $O_2^{\cdot-}$ in plasma (Supplementary Figure S12).

Conclusion

In this case, the SiO_2-$Mn_3(PO_4)_2$ NPs, synthesized *via* self-assembly technique and nanotechnology, were applied in a biomimetic enzyme biosensor for the detection of $O_2^{\cdot-}$. Results revealed that SiO_2-$Mn_3(PO_4)_2$/MWCNTs/GCE showed high electrocatalytic activity toward $O_2^{\cdot-}$, lower detection limit and wide detection range. Furthermore, the biosensor that assembled under optimal conditions exhibited high selectivity of $O_2^{\cdot-}$ in the presence of related interference, such as H_2O_2, UA, AA, DA and Cys. Meanwhile, the long-term stability and good reproducibility of this biomimetic enzyme biosensor were proved. Compared with the $Mn_3(PO_4)_2$ multilayer sheets, the modified GCE of SiO_2-$Mn_3(PO_4)_2$ with high specific surface area exhibited more excellent analytical performance. Consequently, the biomimetic enzyme-free sensor was successfully applied to detecting $O_2^{\cdot-}$ that released from live cells, which holds a great promising platform for the reliable monitoring of major diseases in future.

Methods

Materials. Tetraethyl orthosilicate (TEOS) was purchased from Sinopharm Chemical Reagent Co. Ltd. Cetyltrimethylammonium bromide (CTAB) was obtained from Shanghai Lingfeng Chemical Reagent Co. Ltd. (3-Aminopropyl) triethoxysilane (APTES), phytic acid (PA, 70 wt%) solution and phytic acid sodium salt hydrate

were received from Aladdin Chemistry Co. Ltd (Shanghai, China). Potassium phosphate tribasic trihydrate ($K_3PO_4{\cdot}3H_2O$), manganese sulfate monohydrate ($MnSO_4{\cdot}H_2O$) and dimethyl sulfoxide (DMSO) were obtained from Sinopharm Chemical Reagent Co. Ltd. Potassium hyperoxide (KO_2) was purchased from Alfa Aesar. Multi-walled carbon nanotubes (MWCNTs) was purchased from Shenzhen Nanotech Port Co. Ltd. Triton X-100, nafion (5 wt% solution in lower aliphatic alcohol), 18-crown-6, phorbol 12-myristate 13-acetate (PMA), dopamine (DA), cysteine (Cys), ascorbic acid (AA) and uric acid (UA) were acquired from Aladdin Sigma-Aldrich Co. (USA). Hydrogen peroxide (H_2O_2, 30%) was received from Beijing Chemical Works (China). Phosphate buffer solution (PBS) was obtained by dissolving 8.0 g NaCl, 0.2 g KCl, 1.44 g NaH_2PO_4 and 0.24 g KH_2PO_4 in 1000 mL double-distilled water.

Apparatus. The morphologies of the samples were recorded by transmission electron microscopy (TEM) and high-resolution transmission electron microscopy (HITACHI H-7650, Japan). Scanning electron microscope (SEM) images were obtained by a Scanning electron microscope (JSM-6300, Japan). XPS measurements were performed on a Thermo ESCALAB 250 using a monochromic Al X-ray source (1486.6 eV). All the electrochemicals data were measured by CHI 760D electrochemical workstation (Shanghai Chenhua, China). Fourier transform infrared (FTIR) spectra of the SiO_2 NPs and SiO_2-PA NPs were obtained from a VARIAN Cary 5000 Fourier transform infrared spectrophotometer (VARIAN, USA). Surface potential of the samples was performed by Zeta potential analyzer (Malvern Instruments ZS90). All experiments were carried out using a three-electrode cell equipped, which consisted of a platinum electrode, saturated calomel electrode (SCE) and working electrode.

Culture of Cells. The HeLa cells were cultured in Dulbecco's Modified Eagle's medium (DMEM) containing 10% fetal bovine serum (FBS), 100 units·mL^{-1} penicillin, and 100 μg·mL^{-1} streptomycin at 37 °C. Then, the HeLa cells were centrifuged for the electrochemical experiments. Real sample measurements were performed by the addition of 100 μg·mL^{-1} PMA in PBS containing 50 mM glucose.

Preparation of SiO_2-$Mn_3(PO_4)_2$ NPs. Firstly, SiO_2 NPs were synthesized by the reverse microemulsion method as reported previously by Bagwe[48]. In a typical synthesis, triton X-100 (10.62 g), hexanol (9.6 mL) and cyclohexane (45 mL) were mixed in a 100 mL round-bottomed flask under stirring for 10 min, and then water (2.88 mL) was added to the mixture at room temperature. After being stirred for 0.5 h, $NH_3{\cdot}H_2O$ (600 μL) and TEOS (1200 μL) were dropped into the above clear solution, respectively. Next, the mixture was allowed to stir for a further 24 h at room temperature. The resulting NPs were collected by centrifugation and dried at 60 °C under vacuum condition for 24 h. Then, the modified process of SiO_2 was briefly described as follows: SiO_2 NPs (0.05 g) was dissolved in double-distilled water (20 mL), and TEOS (100 μL) was added to the SiO_2 suspension with continuously stirring for 30 min at room temperature[49]. Then, the SiO_2-NH_2 NPs were obtained by feeding appropriate amount of APTES. After stirring for 30 min, 120 μL of PA/PA sodium salt hydrate buffer solution (pH = 7) was injected into the above solution with continues stirring for 24 h. The resulting NPs were washed with alcohol and double-distilled water. Finally, the SiO_2-PA NPs were redispersed in water (10 mL), and then $MnSO_4$ aqueous solution (10 mL, 12 mM) was injected to the round-bottomed flask containing the SiO_2-PA NPs under constant stirring for 1 h at 60 °C. After completion of the reaction, the obtained products were collected by centrifugation, washed with double-distilled water, and dried in a vacuum oven at 60 °C for 24 h.

Fabrication of SiO_2-$Mn_3(PO_4)_2$/MWCNTs/GCE. Firstly, MWCNTs (8.0 μL, 2.5 mg·mL^{-1}) were cast onto the electrode surface and dried at room temperature. After that, SiO_2-$Mn_3(PO_4)_2$ (8.0 mg·mL^{-1}) and 2.5% Nafion with the volumetric ratio of 1:1 were mixed, and 8.0 μL of above solution was dropped onto the surface of MWCNTs/GCE. After drying in air, the SiO_2-$Mn_3(PO_4)_2$/MWCNTs/GCE was obtained. During the experimental period, the modified electrodes were stored at 4 °C until use.

Generation of superoxide anion. A stable $O_2^{\cdot-}$ solution was prepared by dispersing KO_2 to DMSO (containing 18-crown-6). In accordance with the molar absorptivity of $O_2^{\cdot-}$ in DMSO, the concentration of $O_2^{\cdot-}$ was monitored by recording the absorbance of ferricytochrome c spectrophotometrically at 550 nm[50]. In particular, spectrophotometric measurement of the amount of ferricytochrome c that reduced by $O_2^{\cdot-}$ referred to the following reaction: cytochrome c (Fe^{III}) + $O_2^{\cdot-}$ = ferrocytochrome c (Fe^{II}) + O_2, in which ferrocytochrome c exhibits a strong absorbance at 550 nm[51]. The linear relationship of the absorbance *vs* the ferrocytochrome c concentration was depicted in Figure S13. The linear equations were $A_{550} = 20.6c - 0.0044$, $R = 0.9986$. The concentration of $O_2^{\cdot-}$ can be calculated by the concentration of the formed ferrocytochrome c according to the above reaction formula[52].

References

1. Tian, Y., Mao, L. Q., Okajima, T. & Ohsaka, T. Superoxide dismutase-based third-generation biosensor for superoxide anion. *Anal. Chem.* **74,** 2428–2434 (2002).
2. Karakoti, A. *et al.* Redox-active radical scavenging nanomaterials. *Chem. Soc. Rev.* **39,** 4422–4432 (2010).
3. Zhang, W. *et al.* Elucidating the relationship between superoxide anion levels and lifespan using an enhanced two-photon fluorescence imaging probe. *Chem. Commun.* **51,** 9710–9713 (2015).
4. Wang, Q., Yang, X. Q. & Qu, D. Y. *In situ* ESR spectro-electrochemical investigation of the superoxide anion radical during the electrochemical O_2 reduction reaction in aprotic electrolyte. *Carbon* **61,** 336–341 (2013).
5. Pieta, P., Petr, A., Kutner, W. & Dunsch, L. In situ ESR spectroscopic evidence of the spin-trapped superoxide radical, $O_2^{\cdot-}$, electrochemically generated in DMSO at room temperature. *Electrochim. Acta* **53,** 3412–3415 (2008).
6. He, W. *et al.* Intrinsic catalytic activity of Au nanoparticles with respect to hydrogen peroxide decomposition and superoxide scavenging. *Biomaterials* **34,** 765–773 (2013).

7. Liu, S. *et al.* Ultrahigh performance liquid chromatography-triple quadrupole mass spectrometry inhibitors fishing assay: A novel method for simultaneously screening of xanthine oxidase inhibitor and superoxide anion scavenger in a single analysis. *Anal. Chim. Acta* **715,** 64–70 (2012).
8. Li, N. *et al.* A highly selective and sensitive nanoprobe for detection and imaging of the superoxide anion radical in living cells. *Chem. Commun*. **48,** 2507–2509 (2012).
9. Naito, K., Tachikawa, T., Fujitsuka, M. & Majima, T. Single-molecule observation of photocatalytic reaction in TiO_2 nanotube: importance of molecular transport through porous structures. *J. Am. Chem. Soc.* **131,** 934–936 (2009).
10. Hu, J. J. *et al.* Fluorescent probe HKSOX-1 for imaging and detection of endogenous superoxide in live cells and *in vivo*. *J. Am. Chem. Soc.* **137,** 6837–6843 (2015).
11. Tsukagoshi, K., Taniguchi, T. & Nakajima, R. Analysis of antioxidants using a capillary electrophoresis with chemiluminescence detection system. *Anal. Chim. Acta* **589,** 66–70 (2007).
12. Diez, L. *et al.* High-performance liquid chromatographic assay of hydroxyl free radical using salicylic acid hydroxylation during *in vitro* experiments involving thiols. *J. Chromatogr. B* **763,** 185–193 (2001).
13. Gao, X., Ding, C. Q., Zhu, A. W. & Tian, Y. Carbon-dot-based ratiometric fluorescent probe for imaging and biosensing of superoxide anion in live cells. *Anal. Chem*. **86,** 7071–7078 (2014).
14. Yu, F. B., Gao, M., Li, M. & Chen, L. X. A dual response near-infrared fluorescent probe for hydrogen polysulfides and superoxide anion detection in cells and *in vivo*. *Biomaterials* **63,** 93–101 (2015).
15. Tachikawa, T., Wang, N., Yamashita, S., Cui, S. C. & Majima, T. Design of a highly sensitive fluorescent probe for interfacial electron transfer on a TiO_2 surface. *Angew. Chem. Int. Edit*. **49,** 8593–8597 (2010).
16. Walkey, C. *et al.* Catalytic properties and biomedical applications of cerium oxide nanoparticles. *Environ. Sci.: Nano* **2,** 33–53 (2015).
17. Gale, E. M. *et al.* Toward functional Ni-SOD biomimetics: achieving a structural/electronic correlation with redox dynamics. *Inorg. Chem*. **50,** 9216–9218 (2011).
18. Cheng, H. J. *et al.* Integrated nanozymes with nanoscale proximity for in vivo neurochemical monitoring in living brains. *Anal. Chem.*, doi: 10.1021/acs.analchem.6b00975 (2016).
19. Wei, Hui. & Wang, E. K. Nanomaterials with enzyme-like characteristics (nanozymes): next-generation artificial enzymes, *Chem. Soc. Rev.* **42,** 6060–6093 (2013).
20. He, W. *et al.* Enzyme-like activity of nanomaterials, *J. Environ. Sci. Heal. C* **32,** 186–211 (2014).
21. Wang, X. Y., Hu, Y. H. & Wei, H. Nanozymes in bionanotechnology: from sensing to therapeutics and beyond. *Inorg. Chem. Front.* **3,** 41–60 (2016).
22. Deng, Z., Rui, Q., Yin, X., Liu, H. & Tian, Y. In vivo detection of superoxide anion in bean sprout based on ZnO nanodisks with facilitated activity for direct electron transfer of superoxide dismutase. *Anal. Chem.* **80,** 5839–5846 (2008).
23. Hu, F. X. *et al.* Living cells directly growing on a DNA/Mn3(PO4)2-immobilized and vertically aligned CNT array as a free-standing hybrid film for highly sensitive *in situ* detection of released superoxide anions. *Adv. Funct. Mater.* **25,** 5924–5932 (2015).
24. Barnese, K., Gralla, E. B., Cabelli, D. E. & Valentine, J. S. Manganous phosphate acts as a superoxide dismutase. *J. Am. Chem. Soc.* **130,** 4604–4606 (2008).
25. Ma, X. Q. *et al.* DNA-templated biomimetic enzyme sheets on carbon nanotubes to sensitively *in situ* detect superoxide anions released from cells. *Adv. Funct. Mater.* **24,** 5897–5903 (2014).
26. Yuan, L. *et al.* Biomimetic superoxide dismutase stabilized by photopolymerization for superoxide anions biosensing and cell monitoring. *Anal. Chem*. **86,** 4783–4790 (2014).
27. Cheang, T. Y. *et al.* Promising plasmid DNA vector based on APTES-modified silica nanoparticles. *Int. J. Nanomed.* **7,** 1061–1067 (2012).
28. Hsiao, V. K. *et al.* Aminopropyltriethoxysilane (APTES)-functionalized nanoporous polymeric gratings: fabrication and application in biosensing. *J. Mater. Chem.* **17,** 4896–4901 (2007).
29. Zhao, W. B. *et al.* Innovative biocompatible nanospheres as biomimetic platform for electrochemical glucose biosensor. *Biosens. Bioelectron*. **44,** 1–5 (2013).
30. Dong, J. *et al.* A nanoporous zirconium phytate film for immobilization of redox protein and the direct electrochemical biosensor. *Sensor Actuat. B* **150,** 141–147 (2010).
31. Tang, F. *et al.* Phytic acid doped nanoparticles for green anticorrosion coatings. *Colloid Surface A* **369,** 101–105 (2010).
32. Sun, C. *et al.* Hemocompatible and antibiofouling PU-F127 nanospheres platform for application to glucose detection in whole blood. *J. Mater. Chem. B* **1,** 801–809 (2013).
33. Maji, S. K. *et al.* Immobilizing gold nanoparticles in mesoporous silica covered reduced graphene oxide: A hybrid material for cancer cell detection through hydrogen peroxide sensing. *ACS Appl. Mater. Interfaces* **6,** 13648–13656 (2014).
34. Cao, H. M. *et al.* Protein-inorganic hybrid nanoflowers as ultrasensitive electrochemical cytosensing Interfaces for evaluation of cell surface sialic acid. *Biosens. Bioelectron*. **68,** 329–335 (2015).
35. Aravindan, V. *et al.* Influence of carbon towards improved lithium storage properties of Li_2MnSiO_4 cathodes. *J. Mater. Chem*. **21,** 2470–2475 (2011).
36. Stankovich, S. *et al.* Graphene-based composite materials. *Nature* **442,** 282–286 (2006).
37. Luo, Y. P., Tian, Y. & Rui, Q. Electrochemical assay of superoxide based on biomimetic enzyme at highly conductive TiO_2 nanoneedles: from principle to applications in living cells. *Chem. Commun.* **21,** 3014–3016 (2009).
38. Zhou, J. Q. *et al.* A reliable and durable approach for real-time determination of cellular superoxide anion based on biomimetic superoxide dismutase stabilized by a zeolite. *Analyst* **136,** 1594–1598 (2011).
39. Preda, G. *et al.* Formation of superoxide anions on ceria nanoparticles by interaction of molecular oxygen with Ce^{3+} sites. *J. Phys. Chem. C* **115,** 5817–5822 (2011).
40. Barroso, M. F., Delerue-Matos, C. & Oliveir, M. B. P. P. Electrochemical DNA-sensor for evaluation of total antioxidant capacity of flavours and flavoured waters using superoxide radical damage. *Biosens. Bioelectron*. **26,** 3748–3754 (2011).
41. Zhu, X., Niu, X. H., Zhao, H. L., Tang, J. & Lan, M. B. Immobilization of superoxide dismutase on Pt-Pd/MWCNTs hybrid modified electrode surface for superoxide anion detection. *Biosens. Bioelectron*. **67,** 79–85 (2015).
42. Wang, L. *et al.* A novel amperometric biosensor for superoxide anion based on superoxide dismutase immobilized on gold nanoparticle-chitosan-ionic liquid biocomposite film. *Anal. Chim. Acta* **758,** 66–71 (2013).
43. Liu, H. Q., Tian, Y. & Xia, P. P. Pyramidal, rodlike, spherical gold nanostructures for direct electron transfer of copper, zinc-superoxide dismutase: application to superoxide anion biosensors. *Langmuir* **24,** 6359–6366 (2008).
44. Tang, J. *et al.* Anamperometric superoxide anion radicalbiosensor based on SOD/PtPd-PDARGO modified electrode. *Talanta* **137,** 18–24 (2015).
45. Luo, Y. P. *et al.* A biomimetic sensor for the determination of extracellular $O_2^{\cdot-}$ using synthesized Mn-TPAA on TiO_2 nanoneedle film. *Biosens. Bioelectron*. **29,** 189–194 (2011).
46. Wang, T., Peng, Z., Wang, Y., Tang, J. & Zheng, G. MnO Nanoparticle@mesoporous carbon composites grown on conducting substrates featuring high-performance lithium-ion battery, supercapacitor and sensor. *Sci. Rep*. **3,** 2693 (2013).
47. Zhang, W. *et al.* Prussian blue banoparticles as multienzyme mimetics and reactive oxygen species scavengers. *J. Am. Chem. Soc.*, doi: 10.1021/jacs.5b12070 (2016).
48. Bagwe, R. P., Hilliard, L. R. & Tan, W. Surface modification of silica nanoparticles to reduce aggregation and nonspecific binding. *Langmuir* **22,** 4357–4362 (2006).

49. Zhao, W. B. *et al.* Laccase biosensor based on phytic acid modification of nanostructured SiO_2 surface for sensitive detection of dopamine. *Langmuir* **30,** 11131–11137 (2014).
50. Thandavan, K., Gandhi, S., Sethuraman, S., Rayappan, J. B. B. & Krishnan, U. M. A novel nano-interfaced superoxide biosensor. *Sensor Actuat. B* **176,** 884–892 (2013).
51. Tian, Y. *et al.* A facilitated electron transfer of copper-zinc superoxide dismutase (SOD) based on a cysteine-bridged SOD electrode. *Biochimica et Biophysica Acta* **1569,** 151–158 (2002).
52. Hirata, F. & Hayaishi, O. Studies on indoleamine 2,3-dixygenase. I. Superoxide anion as substrate. *J. Biol. Chem.* **250,** 5960–5966 (1975).

Acknowledgements

This work was supported by Jiangsu Collaborative Innovation Center of Biomedical Functional Materials, National Natural Science Foundation of China (21571104, 2015M580446), Natural Science Foundation of and Jiangsu Province of China (BK 20131396), and the Priority Academic Program Development of Jiangsu Higher Education Institution.

Author Contributions

C.M. and M.W. proposed and supervised the project. X.S. and F.W. wrote the main manuscript text and discussed the results and experimental conditions with all other authors. X.S., Q.W. and L.M. designed and set up the experimental setup. X.S., Q.W., W.X. and Y.L. carried out the experiments. X.S., W.X. and S.F. designed and carried out the data analysis. All authors have given approval to the final version of the manuscript.

Additional Information

Supplementary information accompanies this paper at http://www.nature.com/srep

Competing financial interests: The authors declare no competing financial interests.

How to cite this article: Shen, X. *et al.* Manganese Phosphate Self-assembled Nanoparticle Surface and Its application for Superoxide Anion Detection. *Sci. Rep.* **6**, 28989; doi: 10.1038/srep28989 (2016).